

## THE VARIETIES OF SYMMETRIC STELLAR RINGS AND RADIAL CAUSTICS IN GALAXY DISKS

CURTIS STRUCK-MARCELL AND PNINA LOTAN

Astronomy Program, Physics Department, Iowa State University

Received 1988 June 23; accepted 1990 January 16

### ABSTRACT

Numerical restricted three-body and analytic calculations are used to study the formation and propagation of cylindrically symmetric stellar ring waves in galaxy disks. These calculations assume a number of different gravitational potentials or potential components in the target galaxies, including softened point-mass, Hubble-like, and Plummer potentials, exponential disks, and a nearly isothermal halo. A variety of ring morphologies are found depending on the collisional disturbances amplitude, and the form of the potentials. Alternately, the models suggest that morphological features, including the number of separate nonoverlapping stellar rings, ring widths, and ring-to-ring separations, can provide useful information about the gravitational potential in ring galaxies.

The inner and outer edges of stellar rings are recognized as (phase-space) fold singularities or catastrophes, which form at cusp singularities. The application of singularity theory techniques to the kinematic radial oscillation model for rings of Lynds and Toomre allows the analytic derivation of ring formation time; ring width as a function of time, position, ring number, and collisional perturbation amplitude; and the relative over-densities of rings versus inter-ring regions. Good agreement is found between the analytic and numerical results.

*Subject headings:* galaxies: interactions — galaxies: internal motions — galaxies: structure — stars: stellar dynamics

### I. INTRODUCTION

#### *a) Ring Galaxy Theory*

The basic collisional model of ring galaxies was presented by Lynds and Toomre (1976) and Theys and Spiegel (1976), and elaborated by Toomre (1978). The model resolved the mystery of the ring in the famous Cartwheel galaxy and implied that other rings with nearby companions are likely to be collision remnants. The publication of the Arp and Madore (1987) catalog greatly increases the number of cataloged ring galaxies and emphasizes the variety of ring morphologies. Since Toomre's pioneering work, there has been little systematic theoretical exploration of the dependence of ring morphology on the orbital and structural parameters of the colliding galaxies. Yet several recent papers (Hernquist and Quinn 1988; Huang and Stewart 1988; Wallin and Struck-Marcell 1988; Appleton and James 1989; Lotan and Struck-Marcell 1990) indicate that a variety of unusual morphologies—including thick rings, “diamond” rings, and outer disk ripples—might be the result of collisions like those that produce more “classical” ring galaxies. This point is demonstrated and extended with additional examples of collisional morphology by the numerical restricted three-body simulations presented in §§ III and IV.

Lynds and Toomre (1976) noted that the basic ring phenomenon results from the simple kinematic epicyclic oscillations following an impulsive disturbance. This suggests that it would be worthwhile to pursue and test analytic results based on the Toomre kinematic model, as well as to compare them to numerical simulations. Such a comparison clarifies the degree to which the kinematical model can be applied to real disk galaxies and helps to understand the results of the numerical simulations themselves. The latter point is particularly important since only a finite number of simulations can be carried

out in the large parameter space. These analytic, kinematic models are described in §§ II and III and compared to numerical results in §§ III and IV. In applying these analytic models, we make use of several techniques from singularity or catastrophe theory.

#### *b) Insights from Singularity Theory*

Substantial advances have been made in the last two decades in understanding the complex dynamics of galaxy interactions, largely as a result of the efforts of numerical experiments (see the reviews of Tremaine 1981; White 1982). On the other hand, the literature shows the continuing importance of analytic approximations that were summarized as early as Chandrasekhar's (1943) text (see, e.g., the review of Toomre 1977; Tremaine 1981). Both the analytic dynamical friction formula and the impulse approximation have provided yardsticks with which to measure the validity of numerical simulations, or to estimate the importance of one process relative to the others at work in a given simulation. Unfortunately, the competing nonlinear processes, both stellar and gasdynamical, that come into play in galaxy interactions hinder the application of analytic theory. However, this is a time of great progress in the mathematical theory of nonlinear systems. The application of some of the new mathematical results and techniques should yield new insights into the dynamics of interacting galaxies.

An important step in this direction was taken by Arnold, Shandarin, and Zel'dovich (1982, hereafter ASZ; see also Shandarin and Zel'dovich 1984). They discussed the structure of the various one- and two-dimensional elementary singularities or catastrophes that develop in the nonlinear collapse of collisionless dark matter “particles” in the galaxy formation epoch. These singularities are curves or surfaces of formally infinite density. In reality, ensembles of particles with nonzero velocity

dispersion could have a large but finite density. This large density makes it plausible to identify the first collapsed structures in the universe with these singularities.

Although the equations studied in ASZ are specific to the cosmological problem, the singularity (or catastrophe) theory approach is much more general (see, e.g., Arnold 1984, 1986; Arnold, Gusein-Zade, and Varchenko 1985; Golubitsky and Schaffer 1985; Majthay 1985; Poston and Stewart 1978). The essence of this approach is the study of the formation and propagation of density singularities in the mass continuity equation, using the equation of motion. Since the focus of this method is on intrinsically nonlinear structures, it bears little conceptual relation to the widely used linear perturbation techniques. However, because galaxy interactions and collisions are also intrinsically nonlinear phenomena, there is a strong motivation to test the applicability of singularity theory techniques. The ring galaxy phenomenon offers perhaps the simplest such application.

On the other hand, it must be admitted at the outset that the Zel'dovich case is an example of a "Lagrangian" system (see Arnold 1980), and the singularities of Lagrangian systems are relatively easy to isolate and study. Specifically, the essential feature of Zel'dovich systems is that the spatial dependences of any perturbation decouple from the temporal development, so that these variables can be separated. This is not generally the case in stellar dynamics, and obviously it is not the case for any nonlinear hydrodynamic wave. However, defining an appropriate generalized time or phase variable (e.g., action-angle variables) can often reveal the Lagrangian nature and separability of many such problems, at least locally. Moreover, in non-Lagrangian systems, the singularity theory outlook may prove useful even if explicit closed-form calculations cannot be carried out.

### c) Outline

The remainder of this paper is divided into six sections as follows. In § II the basic analytical approximations with a softened point mass potential are presented, and the singularity conditions are derived. The results of restricted three-body numerical simulations with single-component potentials are presented in § III. The basic propagation characteristics and parameter dependences of the ring singularities or caustics formed in the simulations are also discussed and compared to the semianalytic models. The dependence of these properties on the radial form of the gravitational potential and potentials with multiple components is discussed in § IV. The comparison of models to observation is discussed in § V. Section VI summarizes the results.

## II. ANALYTIC APPROXIMATIONS

In this section we review simple analytic models for the case of a direct collision between a rotating disk and a companion traveling along the disk symmetry axis, where both galaxies have time-independent potential. (Thus we assume that the change in the galaxy potentials in the encounter has a negligible effect on the subsequent evolution of the target disk.) As a specific example, we will study the case of a family of potentials that includes both the softened point-mass and the Plummer potential, and in later sections we will give brief results for other potentials. The acceleration of a point particle in these potentials is given by

$$g = \frac{-GMr^{2p-2}}{(r^2 + \epsilon^2)^p}, \quad (1)$$

where  $\epsilon$  is the softening length of the potential, and we assume  $p \geq 1$  ( $p = 1$  is the softened point-mass potential, and  $p = 3/2$  is the Plummer potential). The advantage of this form is that it is relatively simple but still possesses a rotation curve with qualitative features similar to those observed in many disk galaxies. These include the following: (1) an increasing rotation velocity as a function of radius at small radii, (2) a fairly broad turnover region which mimics a flat rotation curve, and (3) a Keplerian falloff at radii much larger than the softening length. Another practical advantage of these potentials is that they have been used frequently in numerical simulations.

### a) The Disturbance

We will consider two limiting types of disturbance which are simple enough to allow an explicit estimate of the magnitude of the disturbance caused by the intruder galaxy on the stellar orbits in the target galaxy. The first of these special cases is the usual impulse approximation, where it is assumed that the disturbance occurs very rapidly relative to stellar orbital or relaxation times (see, e.g., Alladin 1965; Toomre 1977; Tremaine 1981).

Consider the case of an intruder moving rapidly along the disk symmetry axis. In the impulse approximation, the star's position changes negligibly during the encounter and is treated as a fixed number. The net change in the velocity of a star located in the plane of the disk at a position  $(x, y, 0)$  due to an intruder of mass  $M_c$  moving on the disk symmetry axis is

$$\Delta v = \frac{-2GM_c}{rV_{\text{rel}}} \hat{r}, \quad (2)$$

where  $r = (x^2 + y^2)^{1/2}$ , and where  $V_{\text{rel}}$  is the relative velocity between the mass  $M_c$  and the disk galaxy.

Among the problems in applying the impulse approximation to head-on collisions is the fact that most collisions are more likely to be marginally bound, rather than highly unbound (e.g., Chatterjee 1987). Thus, the underlying notion of an instantaneous, impulsive hit is not correct. This fact does not necessarily make it impossible to approximate the disturbance, but the approximation must be based on slightly different assumptions. Specifically, if the collision occurs on a time scale comparable to the epicyclic period of a fiducial star, we expect roughly the following sequence of events. First, the star falls inward in response to the additional gravity of the companion as the latter approaches the disk center. Once the companion passes through the center, the star continues to fall inward against the centrifugal barrier until it is brought to rest. By this time, the companion is far enough away that its gravity is unimportant relative to the unbalanced centrifugal force, so the star is released to pursue epicyclic oscillations. In this picture, unlike the impulse case, the star has time to respond to the disturbance, although not sufficiently slowly to preserve adiabatic invariants.

In a collision where the following conditions are satisfied: (i) the collision is axisymmetric or nearly so, (ii) the perturbation on a disk star in the target galaxy is small enough that the star remains approximately confined to the disk plane, then the *magnitude* of the total angular momentum is approximately conserved. This fact can be used as the basis for a simple analytic estimate for the amplitude of the epicyclic motion of a star in the disk plane in response to the perturbation. To begin, we assume that the star's minimum radius is the point where the centrifugal force would balance both the disk galaxy

gravity and the companion's gravity when it is located at the disk center. This approximation is likely to lead to a slight overestimate of the disturbance (as can be seen in the numerical hydrodynamical simulations of Struck-Marcell and Appleton 1987 [Paper II]). Under these assumptions, the radial force balance equation for the star at minimum radius is approximately

$$\frac{-GM_c}{r^2} - \frac{GM_r^{2p-2}}{(\epsilon^2 + r^2)^p} + \frac{h^2}{r^3} = 0, \quad (3)$$

where subscript  $c$  refers to the intruding companion, and  $h$  is the magnitude of the angular momentum per unit mass of the star in the target disk. Using the initial unperturbed force balance equation (e.g., eq. [3] with  $M_c = 0$ ), we can eliminate  $h$  in equation (3). Then, letting  $\xi = r/q$ , where  $q$  is the initial unperturbed position of the disk star (following Zel'dovich's notation for the Lagrangian coordinate), we have the following equation for  $\xi$ ,

$$-\left(\frac{M_c}{M}\right)\xi\left(\frac{\epsilon^2}{q^2} + \xi^2\right)^p - \xi^{2p+1} + \left[\frac{(\epsilon^2/q^2) + \xi^2}{(\epsilon^2/q^2) + 1}\right]^p = 0. \quad (4)$$

In the limit that  $q \gg \epsilon$ , the gravity of the parent galaxy reduces to Keplerian form, so that to first order in  $\epsilon/q$  the expression for the oscillation amplitude is the same as that for a point mass (i.e., no  $\epsilon/q$  term), and is given by

$$\frac{\delta r}{q} = 1 - \xi = \frac{(M_c/M)}{1 + (M_c/M)} \quad (5)$$

Thus, under the above assumptions, the disturbance is independent of the initial position  $q$  within the target disk. (Note also the difference of a factor of 2 from eq. [A2] in Struck-Marcell and Appleton 1987, which is in error.) The opposite limit,  $q \ll \epsilon$ , is dependent on the companion potential, and it does in general depend on  $q$ .

Equation (2) gives  $\Delta v$  in the impulse approximation, and the parallel expression in the present centrifugal balance approximation can be derived as follows:  $\Delta v \propto \delta r/\Delta t \propto q/\Delta t$  (using eq. [5]). Also  $\Delta t \propto 1/\omega$ , and  $\omega \propto (GM_g/q^3)^{1/2}$  (see eq. [8] below when  $q/\epsilon \gg 1$ ). Therefore,  $\Delta v \propto (GM_g/q)^{1/2}$ . A comparison between this expression and equation (2) indicates that the disturbance in the outer disk is much greater in this case than in the impulse approximation. Therefore, a significant amount of (orbital) energy is deposited in the outer disk whenever this approximation is valid. Note that the solution to equation (4) is also the equilibrium radius of a disk star following an axisymmetric merger with the companion.

With the results above, we can describe the perturbation amplitude in a variety of limiting cases. However, in most of the analytic work below we will limit ourselves to the simple approximation that the perturbation amplitude is a constant independent of radius. This approximation is not very accurate in the inner parts of the disk, but we have no special interest in those regions in this work. As a heuristic exploration of the possible dynamical behaviors, this approximation will suffice.

#### b) Stellar-Free Oscillations in a Simple Potential

In response to a low-amplitude, quasi-impulsive perturbation, a star in the target disk will execute radial harmonic oscillations in addition to its initial (circular) orbital motion. As a first approximation, we can assume that stars located throughout the disk are essentially noninteracting. The fre-

quencies and relative phases of these epicyclic oscillators, as a function of position within the disk, are the key parameters for determining the structure and evolution of rings or similar waves, as Lynds and Toomre (1976) pointed out.

The oscillation frequency as a function of radius is readily derived from the radial component of the linearized equation of motion (also see Saslaw 1985; Binney and Tremaine 1987). Let the perturbed radius be given by

$$r = q - Aq \sin(\omega t + \phi), \quad (6)$$

where the (constant) amplitude  $A$  equals  $\delta r/q$ . The radial equation of motion is given by

$$\frac{d^2 r}{dt^2} = \frac{-GM_r^{2p-2}}{(r^2 + \epsilon^2)^p} + \frac{h^2}{r^3}, \quad (7)$$

where we take  $h(q)$  to be conserved during the encounter. Substituting equation (6) into equation (7), expanding in powers of the amplitude  $A$ , retaining only terms to first order in  $A$ , and using the equilibrium version of equation (7) ( $d^2 q/dt^2 = 0$ ) leads to the following expression for the epicyclic frequency,

$$\omega^2(q) = \frac{GMq^{2p-3}}{(q^2 + \epsilon^2)^p} \left[ \frac{q^2 + (2p+1)\epsilon^2}{q^2 + \epsilon^2} \right]. \quad (8)$$

Equations (6) and (8) specify the radial kinematics of a disturbed stellar orbit. In exploring the properties of the simple model represented by these two equations, we will make the following simplifications: we set the amplitude  $A$  constant independent of  $q$  throughout the disk as discussed above, and we set all the initial phases  $\phi(q)$  equal to zero (i.e., assume no initial radial motions). Modifications of the approximation are discussed in § IV below. (We note also that eq. [8] corrects an error in eq. [B3] of Appleton and Struck-Marcell.)

#### c) Ring Singularities

It is instructive to compare equation (6) with the Zel'dovich approximate solution for the motion of particles in the collapse of a cosmological overdensity perturbation (eq. [1] of ASZ). Clearly, we do not have the simple separability into a product of distinct functions of  $q$  and  $t$  [i.e., derivatives of the displacement function  $S(q)$  and an evolution function]. However, for some purposes the simple expedient of adopting the phase  $\omega t$  as time coordinate overcomes this difficulty, at least away from extrema of  $\omega(q)$  (see § Vb). Then we can follow ASZ to consider equation (6). "as a one-parameter family of mappings of Lagrangian space (corresponding to the so-called unperturbed state) into an Eulerian one, parameterized by time. These mappings are Lagrangian. Thus, we can use the classification of the singularities of the Lagrangian mappings (Arnold 1972) and the metamorphoses of these singularities" (Arnold 1976).

Mathematically, these singularities or catastrophes are defined in terms of second and higher order derivatives of a displacement function. In a cylindrically symmetric system, the mass continuity equation gives the following expression for the local star density in terms of the initial unperturbed density  $\rho_0(q)$ :

$$\frac{\rho}{\rho_0} = \left( \frac{r}{q} \frac{\partial r}{\partial q} \right)^{-1}. \quad (9)$$

Note that the density formally goes to infinity when

$$\frac{\partial r}{\partial q} = 0. \quad (10)$$



In fact, this condition is equivalent to a zero of a second derivative of the displacement function, and we will henceforth take it as our definition of a singularity. Equation (10) is essentially an orbit crossing or caustic condition for the radial motion, but equation (9) shows that such caustics are also strong density waves. The infinite densities implied for a solution of equation (10) are certainly not realized physically. The finite number of stars in a galactic disk and the fact that the stellar ensemble has a nonzero velocity dispersion are not accounted for in the kinematic motion equation (6). The latter effect will result in a smoothing of sharp density peaks (see § V). In any case, equation (10) determines the Lagrangian mapping which describes the location and structure of strong circular density waves, as will now be shown.

Substituting equation (6) into the caustic condition (10) gives

$$1 - A \sin(\omega_c t) - A q_c t \cos(\omega_c t) \left( \frac{d\omega}{dq} \right)_{q=q_c} = 0. \quad (11)$$

The structure of the gravitational potential of the target galaxy, which must play a key role in determining the propagation of waves and caustics, enters into equation (11) through the radial gradient of the epicyclic frequency. For the potentials specified by equation (1), and using equation (8), this gradient can be written

$$\frac{d\omega}{dq} = - \left( \frac{\omega}{q} \right) \left\{ \frac{3q^4 + 2(4p+3)q^2\epsilon^2 - (2p-3)(2p+1)\epsilon^4}{2(q^2 + \epsilon^2)[q^2 + (2p+1)\epsilon^2]} \right\} \quad (12a)$$

$$= - \left( \frac{\omega}{q} \right) f_1 \left( \frac{q}{\epsilon} \right), \quad (12b)$$

where the function  $f_1$  is defined as the quantity in braces in the first equation. Substituting equation (12) into equation (11), we have

$$f_1 \left( \frac{q_c}{\epsilon} \right) = \frac{A \sin(\omega_c t) - 1}{A \omega_c t \cos(\omega_c t)} = W(A, \omega_c t), \quad (13)$$

where we have written this in a form that reveals the separability into a function  $f_1$  of the unperturbed structure of the galaxy on the left-hand-side and a function  $W$  of the amplitude and frequency on the right-hand side.

Equation (13) is a quadratic equation in the quantity  $(q_c/\epsilon)^2$ , whose solution is

$$\frac{q_c^2}{\epsilon^2} = \frac{2W(p+1) - (4p+3)}{3-2W} \pm \frac{2p^{1/2}}{(3-2W)} \times [pW^2 - 2(3p+1)W + (7p+3)]^{1/2}. \quad (14)$$

Recall that  $q$  is the initial, unperturbed radius or Lagrangian coordinate of the star, which thereafter labels the ensemble of stars located initially at that radius. Equation (14) specifies the location of a caustic in terms of the Lagrangian coordinates of the stars contained within it. The radial position of the caustic is obtained by substituting equation (14) into equation (6). These equations specify  $q_c$  and  $r_c$  as complicated functions of the phase  $\omega t$  (and amplitude  $A$ ). Since  $\omega$  is itself a nontrivial function of  $q$ , equation (14) cannot be solved explicitly for  $q_c(t)$ .

There is some simplification in the limiting cases. First, note that equation (14) has real positive solutions only for  $(3-2p)/2 < W < 3/2$ , and  $3/2 < W < [(3p+1) - (2p^2 + 3p + 1)^{1/2}]/p (\approx 3/2)$ , for  $1 \leq p \leq 3/2$ . Inspection of

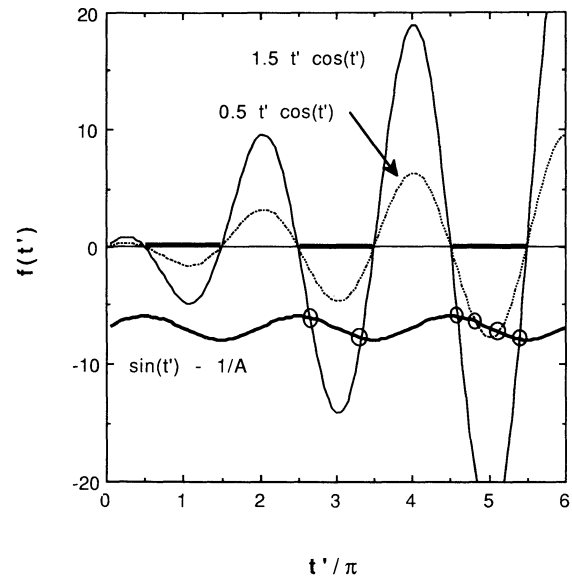


FIG. 1.—Solutions to the caustic condition as a function of oscillation phase in the limiting cases given by eqs. (15) and (16) divided by  $A$  (and with dummy variable  $t' = \omega t$ ). The thick solid curve represents the left-hand side of those equations when the amplitude  $A = 1/2$ . The thin solid and dashed curves represent the right-hand sides of eqs. (15) and (16), respectively. Intersections between the thick curve and either the thin solid curve or the dashed curve imply the existence of caustics in the outer and inner disk, respectively. These intersections are highlighted with open circles. Intersections can only occur in permitted phase intervals which are marked as thick lines on the  $f(\omega t) = 0$  line. For smaller amplitudes  $A$ , the thick curve is translated downward, making caustics less likely in the first few rings, while for larger amplitudes the thick curve is translated upward.

equation (13) reveals that this limitation on  $W$  implies that the cosine in that equation has a negative sign when  $p \leq 3/2$ , and so  $(2n-1)\pi - \pi/2 < \omega t < (2n-1)\pi + \pi/2$ , with  $n = 1, 2, 3, \dots$ . This means that at a given time caustics can only occur for values of  $\omega$  (and therefore  $q$ ) within these intervals.<sup>1</sup> Whether or not caustics actually form within the allowed phase interval depends on the amplitude  $A$  of the perturbation. In any case, each allowed phase interval will be a compressed region, so we will refer to the  $n$ th interval as the  $n$ th ring.

In the limit  $q_c/\epsilon \gg 1$ , equations (12) and (13) reduce to  $W \approx 3/2$ , and

$$A \sin(\omega_c t) - 1 \approx \frac{3}{2} A(\omega_c t) \cos(\omega_c t). \quad (15)$$

On the other hand, if  $q_c/\epsilon \ll 1$ , then  $W \approx (3-2p)/2$ , and

$$A \sin(\omega_c t) - 1 \approx \left( \frac{3-2p}{2} \right) A(\omega_c t) \cos(\omega_c t). \quad (16)$$

Equations (15) and (16) constitute the implicit  $q_c - t$  relation in their respective limits. Unfortunately, even in these limiting cases we cannot separate  $\omega(q_c)$  from  $t$ , to solve explicitly for  $q_c(t)$ . Yet a graphical representation reveals much of the essence of these equations. This is shown in Figure 1 (for the softened point-mass case  $p = 1$ ), where the left-hand side of the equations (divided by  $A = 1/2$ ) is graphed as a thick curve while the right-hand sides are graphed as thin curves. The solid curve corresponds to equation (15), and the dotted curve corre-

<sup>1</sup> If  $p > 3/2$ , it is possible to have inward propagating ring waves with phase  $\omega t$  centered on  $2\pi n$ , rather than  $(2n-1)\pi$ .

sponds to equation (16). The intersections between thick and thin curves mark the solutions to the equations. The thickened intervals on the phase axis designate the allowed regions, where caustics can occur.

#### d) Ring Structure and Fold Singularities

For the arbitrarily chosen amplitude  $A = \frac{1}{2}$  in Figure 1, there are no caustics for the first allowed interval ( $n = 1$ ). There are caustic solutions to equation (16) for  $n = 2$ , but not for equation (15). This suggests the possibility that in some cases a ring may originate in the inner regions as a mere density enhancement, and only later as it propagates to the outer disk, develop caustics. (Such a case is also evident in the second ring for  $A = 0.1$  [solid curve] in Fig. 7 below.) Caustic solutions exist in both cases for higher values of  $n$ , if  $p < 3/2$ . (If  $p = 3/2$ , the Plummer model, caustics can never form in the limit of eq. [16], and if  $p > 3/2$ , inward propagating caustics can form in this limit.<sup>2</sup>) It is also evident from the figure that caustic solutions appear in the intervals corresponding to small values of  $n$  as the amplitude  $A$  is increased. (In the figure, the thick solid curve is pushed upward as the amplitude is increased.) Alternatively, for the  $n$ th interval there exists some minimum value of the amplitude  $A_{\min}^n$  for the appearance of a caustic in that interval. If  $A = A_{\min}^n$ , then the curves for the left-hand side and the right-hand side of equation (15) or (16) will intersect at a point, with  $\omega_c t \approx (2n - 1)\pi$ . For  $A$  slightly greater than  $A_{\min}^n$  there will be paired caustic solutions within the relevant interval, one on each side of the phase  $\omega t = (2n - 1)\pi$ , and quite close to it. These are the inner and outer edges of the ring. We define this phase difference as  $\theta$ , such that  $\omega t = (2n - 1)\pi \pm \theta$ . For  $A$  slightly greater than  $A_{\min}^n$ ,  $\theta$  is small, so we can approximate

$$\sin(\omega t) = \pm \sin(\theta) \approx \pm(\theta - \frac{1}{6}\theta^3),$$

for

$$\theta = \pm[(2n - 1)\pi - \omega t] \quad (17)$$

and

$$\cos(\omega t) = -\cos(\theta) \approx -1 + \frac{1}{2}\theta^2.$$

Substituting  $\omega_c t$  into equation (15) and expanding to third order in  $\theta$  yields

$$\frac{11}{12}(\pm\theta)^3 + \frac{3}{4}\pi(2n - 1)\theta^2 - \frac{1}{2}(\pm\theta) + \frac{1}{A} - \frac{3}{2}(2n - 1)\pi = 0. \quad (18)$$

First of all, we note that if  $\theta = 0$ , this equation implies that  $A_{\min}^n = [3\pi(2n - 1)/2]^{-1}$ , or  $A_{\min}^n = [\pi(2n - 1)(3 - 2p)/2]^{-1}$  if we use equation (16).

These values for  $A_{\min}^n$  imply some interesting consequences for collisions with very low mass companions. For example, with  $M_c/M = 0.05$  and  $p \approx 1$ , we would not expect the caustic condition to be met until the third or fourth ring. Also, the ring would be thin and contain very little mass (see below). These conclusions are confirmed in numerical simulations (described below).

To first order in  $\theta$ , the solution to equation (18) is

$$\pm\theta^{(n)} \approx 2\left(\frac{1}{A} - \frac{1}{A_{\min}^n}\right) = 2\left(\frac{A_{\min}^n - A}{AA_{\min}^n}\right), \quad (19)$$

<sup>2</sup> See footnote 1.

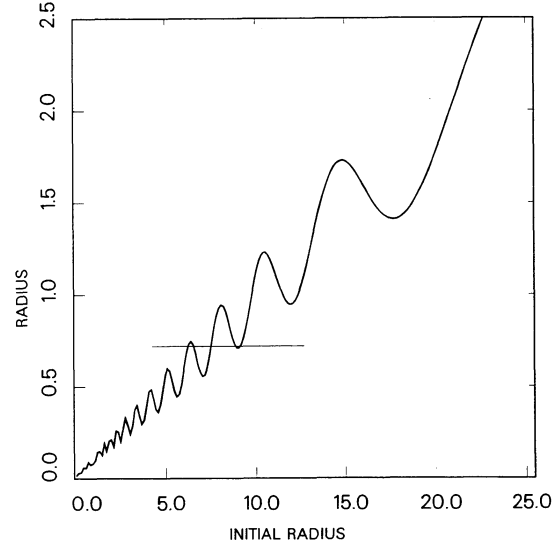


FIG. 2.—Radius  $r(q)$  as a function of initial (Lagrangian) radius  $q$  at a time of  $t = 16\tau_{\text{ff}}$ , with a perturbation amplitude of  $A = 0.2$  ( $p = 1$ ), showing the fold singularities as local peaks and valleys. Values of  $r$  and  $q$  are in units of the softening length  $\epsilon$ . The horizontal line segment shows a region of overlapping rings, where there are five distinct particle streams.

which is a useful estimate for the spreading behavior of the two caustic branches as  $A$  increases beyond  $A_{\min}^n$ . The symmetry between the positive and negative  $\theta$  is retained at least to the second-order solution.

The double-branched nature of the ring caustics is confirmed by Figures 2 and 3, in which equations (6) and (8), with  $A = 0.2$  are plotted in two different ways. Figure 2 shows radius  $r$  as a function of initial radius  $q$  at a fixed (late) time. The singularities are, by definition, points where the curve has zero slope. It is apparent from Figure 2 that, in general, these points come in pairs, as expected. We also can see in Figure 3 that these singularities make up the inner and outer boundaries of the ring, defined as an overdense region.

Figures 2 and 3 (see also Fig. 6 of Toomre 1978) show that there are three streams of particles at any position within a ring. These include (1) stars falling through the ring toward their innermost radius, (2) stars moving up through the ring after reaching their lowest point, (3) stars falling from their maximum radius, back through the ring, and then out through the inner edge of the ring. The three streams reveal these caustics to be type  $A_2$  singularities in the classification of Arnold (1976), or as examples of the fold singularity of catastrophe theory.

Another point that is obvious in Figure 3 is that the outer edge of a high-order ring can move through the inner edge of the previous ring. Figures 1 and 3, as well as equation (19), do indicate (through the dependence of  $A_{\min}^n$  on  $n$ ) that the first few rings will be progressively broader, at least in terms of the opening angle  $\theta$ . More precisely, if we assume that the Lagrangian position of all particles within the ring are roughly equal, then the ring half-width  $\Delta r$  is approximately  $r_c - q$ , namely the difference between the position of a caustic particle and its unperturbed radius. Then, using equations (14), (6), and (17) we get

$$\frac{\Delta r}{\epsilon} = A \frac{q}{\epsilon} \sin(\theta). \quad (20)$$

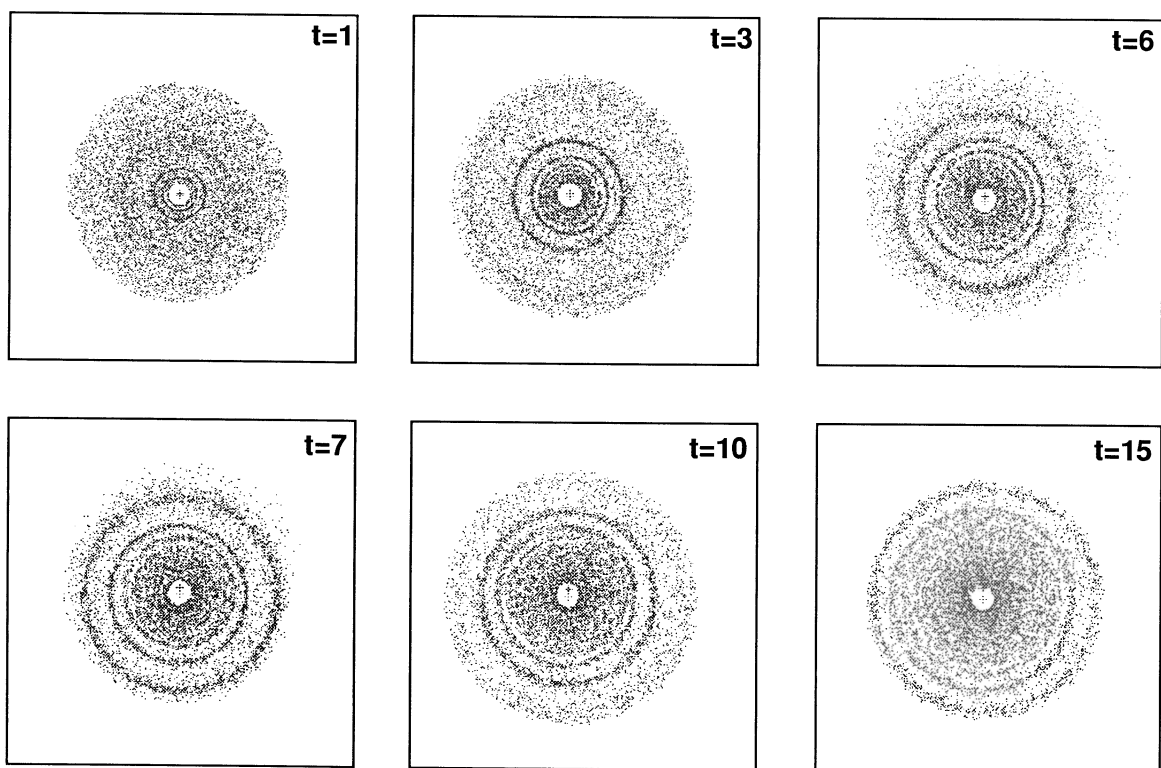


FIG. 4.—Head-on view of a disk consisting of  $10^4$  test particles following the central impact of a 10% mass companion. The potential of the target galaxy consisted of a single Hubble-like bulge component. Time indicated in each snapshot is measured from the moment the companion passes through the disk (see text for details). The radius of the disk is initially  $10\gamma$ , where  $\gamma$  is the potential scale length.

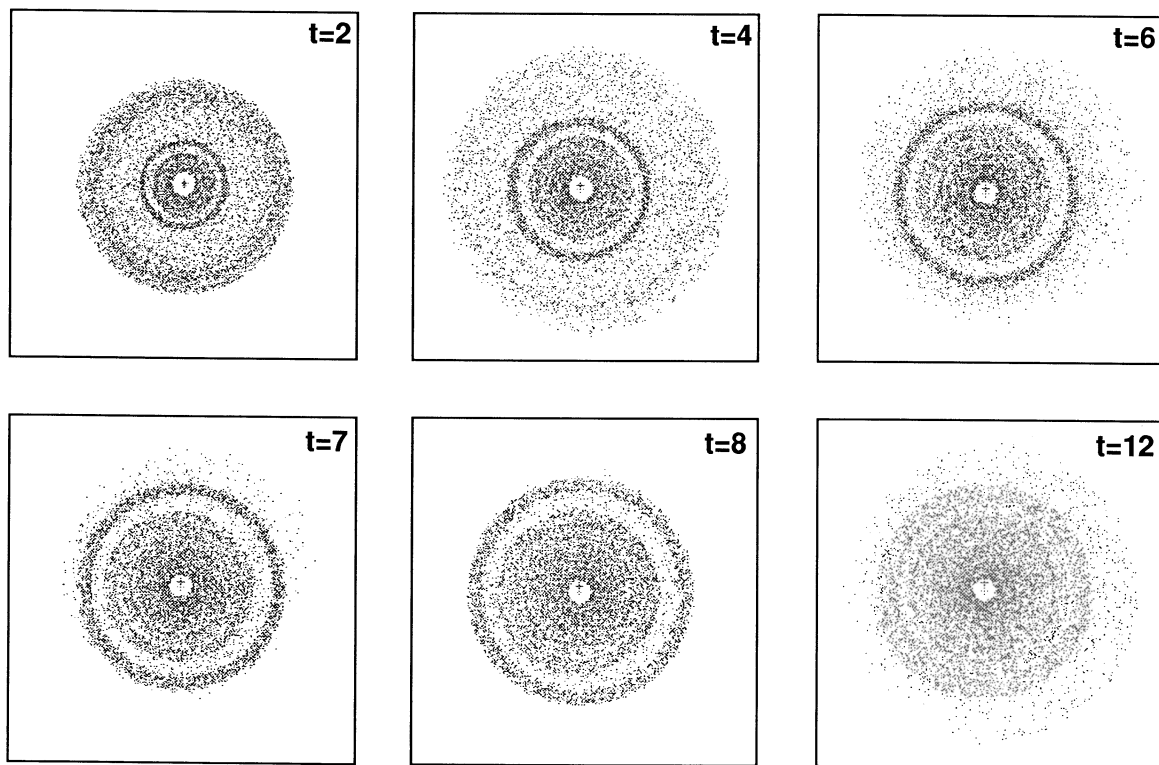


FIG. 5.—Same as Fig. 4, but with a 20% mass companion



similar, as detailed below. In the present work we consider only single encounters, i.e., where the companion orbit is parabolic or hyperbolic and the dynamical friction of the target galaxy is insufficient to drag the companion back over the lifetime of the rings in the disk.

We have constructed a restricted three-body-type code in three dimensions, where the target galaxy is made of three components: bulge, disk, and halo. The potentials of all components are time independent during the entire simulation. This assumption is justified as long as the collisional perturbation is small enough that it does not significantly alter the mass distribution of the colliders. This is probably not accurate for the low-mass companion galaxy, but since we are only interested in the internal structure of the larger target galaxy in this study, and since in the single-pass collision the distortions of the companion probably do not significantly affect how it perturbs the target, the assumption is justified.

The bulge is characterized by a mass density distribution of the form

$$\rho_B(r) = \frac{\gamma}{\pi^2} \frac{M_B}{(r^2 + \gamma^2)^2} \quad (21)$$

(which will be termed a “Hubble-like” profile). The corresponding gravitational acceleration is

$$g_B = \frac{2}{\pi} \frac{GM_B}{r^2} \left[ \frac{r/\gamma}{1 + (r/\gamma)^2} - \tan^{-1} \left( \frac{r}{\gamma} \right) \right]. \quad (22)$$

This density distribution is intermediate between the modified Hubble profile [which goes as  $(r^2 + \gamma^2)^{-3/2}$ ] and the Plummer density profile [which goes as  $(r^2 + \gamma^2)^{-5/2}$ ]. The second component is a three-dimensional disk of mass density

$$\rho(r, z) = \frac{M_D \alpha^2 \beta}{4\pi} \exp(-\alpha r - \beta |z|). \quad (23)$$

The acceleration and potential at any point caused by this component were calculated numerically on a grid, with a three-point interpolation between grid points. The third component is a nearly isothermal halo of mass density distribution,

$$\rho(r) = \frac{\rho_0}{1 + (r/a)^2}, \quad (24)$$

corresponding to the gravitational acceleration,

$$g(r) = \frac{-4\pi G \rho_0 a^3}{r^2} \left[ \frac{r}{a} - \tan^{-1} \left( \frac{r}{a} \right) \right]. \quad (25)$$

In all cases, the companion galaxy is simulated as a single Hubble-like profile (eq. [21]). Some of the simulations were carried out for a target galaxy containing all three (bulge, disk, and halo) components, while others used a single-component target. The multicomponent code is similar to that used by Villumsen (1985). In this method, the centers of mass of the target and intruder are moving in response to their mutual gravity. The origin of the frame of reference is chosen to be the geometrical center of the main galaxy, and therefore a fictitious acceleration term correcting for the noninertial frame of reference is added to the accelerations of all bodies and particles.

The deceleration of the companion due to dynamical friction from the target galaxy is not included. However, unless the companion is merged within the first passage, the mere slowing down has a negligible effect on the response of the target disk

and the characteristics of the propagating rings. This assertion has been confirmed by comparison to simulations including the effects of dynamical friction according to the Chandrasekhar formula.

Each test particle's motion is solely governed by the potentials of the target and companion galaxies, while the gravitational interactions between the test particles (stars) are neglected. The target and companion are extended, and since the companion may also be roughly the same size or mass as the target bulge, the gravitational potential between the two is calculated as that between two interpenetrating clouds with “Hubble-like” mass distributions. In calculating the gravitational potential between the target disk and halo and the companion, the latter is assumed pointlike. The test particles were initially spread in equally spaced annuli in the range  $1-10\gamma$ , each containing the same number of particles (which translates into a  $1/r$  density distribution). All particles were initially located in a perfectly thin disk and assigned velocities consistent with centrifugal balance with the target galaxy potential. In addition, they were given a random velocity component less than or equal to 2% of the scale velocity  $(GM/R_0)^{1/2}$ , where  $R_0 = 10\gamma$  is the initial disk size. Despite the obvious limitations of restricted three-body codes, the potentials used are quite realistic, and thus for reasonably modest perturbations, these simulations can be taken as a standard of comparison for analytic calculations using simple potentials.

In the rest of this section, we will describe simulations done with a target galaxy composed of one component only (Hubble-like or softened point-mass). While these potentials do not accurately represent an entire disk galaxy, they allow closer, more quantitative comparison with the analytic results drawn from the same potentials.

#### b) Numerical Results

Figures 4 and 5 show the development of rings in a target disk consisting of 10,000 test particles following a collision with a 10% and 20% mass companion galaxy, respectively, where both galaxies are dominated by a single Hubble-like bulge component (eq. [21]). In both cases, the companion is in a moderately hyperbolic orbit and impacts the disk perpendicularly at the center.

Figure 4 shows a head-on view of the disk at selected times. Time is measured from the moment the companion passes through the target disk plane. The dimensionless time unit equals  $0.34 (R_0^3/GM)^{1/2}$ . These conventions are followed in Figures 5, 10, and 11 below. In the first snapshot, it can be seen that the first ring has already propagated about halfway through the disk. However, this ring is so faint and diffuse that it is hardly visible until it begins to leave the disk in the second snapshot; as a result, the disk is expanded considerably (compare frames 1 and 2). The second ring has also formed and moved a short ways out from the center. Between times 1 and 10, the second ring propagates through the disk. From early times, it is stronger than the first ring, with quite sharp edges. Note also how it gets steadily thicker as it moves outward. The third ring follows a very similar evolutionary sequence. At late times, there is increasing incoherence in the central regions. Although a fourth ring is discernible, the fifth and higher rings never free themselves from this confusion. Thus, by the last time shown the ringing is almost over, and in later times (not shown) the disk relaxes and smoothes out.

In Figure 5, although the companion is twice as massive, many of the same general features are apparent. The first ring,

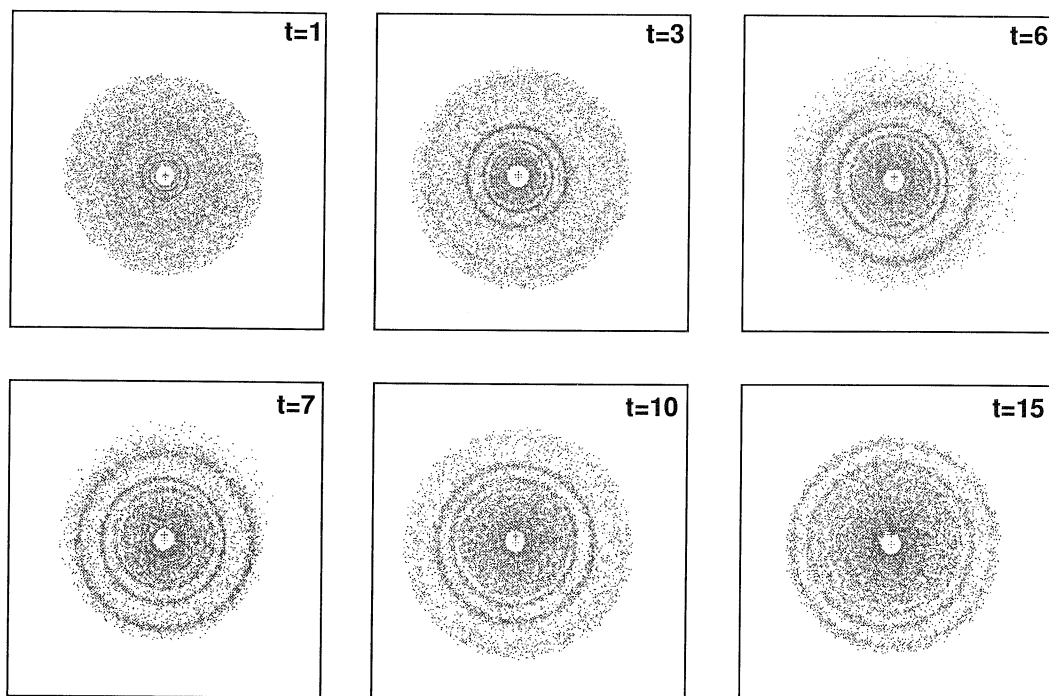


FIG. 4.—Head-on view of a disk consisting of  $10^4$  test particles following the central impact of a 10% mass companion. The potential of the target galaxy consisted of a single Hubble-like bulge component. Time indicated in each snapshot is measured from the moment the companion passes through the disk (see text for details). The radius of the disk is initially  $10\gamma$ , where  $\gamma$  is the potential scale length.

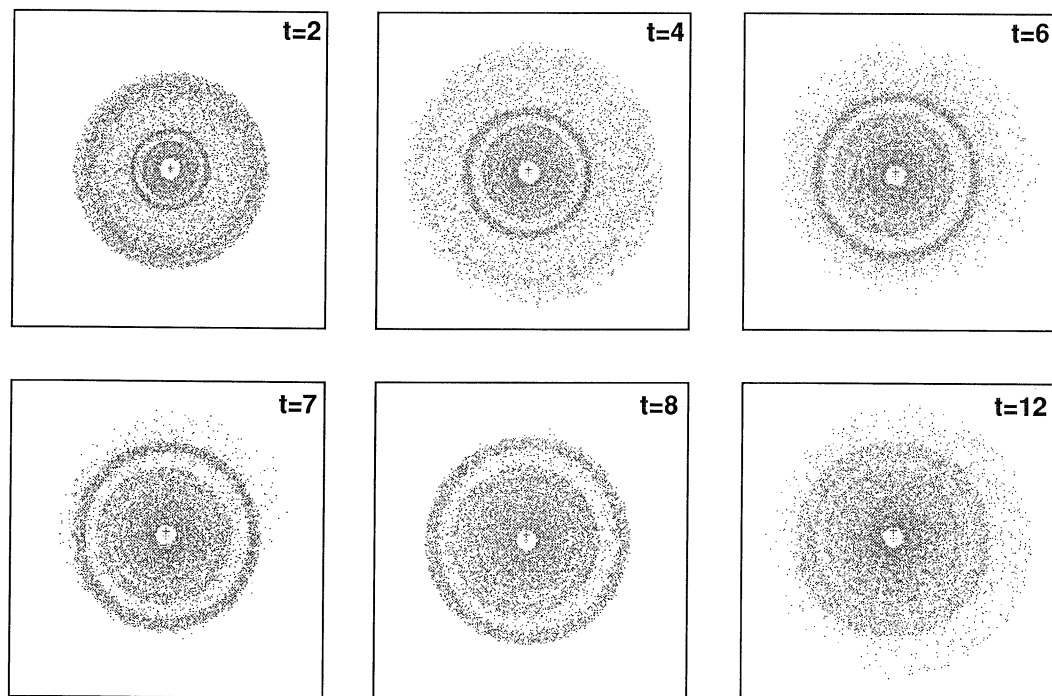


FIG. 5.—Same as Fig. 4, but with a 20% mass companion



which is about to leave the disk in the first frame, is weak (though not *as* weak) and propagates quickly through the disk. The overall size of the disk varies in a similar way. The second ring propagates more slowly than the first and gets thicker as it moves outward.

There are also interesting differences between Figures 4 and 5. The rings are apparently thicker in the latter case, and the density contrasts between ring and inter-ring regions are somewhat greater. Because the rings are substantially thicker in the second case, it is hard to resolve the third and later rings. The incoherence in the central regions sets in earlier, and thus the ringing phenomenon is rendered unrecognizable earlier. This result is interesting because of the somewhat paradoxical implication that larger amplitude disturbances lead to less persistent effects.

The caustics described by equations (6) and (14) can be identified with the inner and outer ring edges in Figures 4 and 5 (see the following section). The finite thermal motions and limited particle resolution prevent these "caustics" from being infinite density surfaces in the numerical simulations, but the abrupt density change at these boundaries is obvious. It appears that the density within the rings is relatively constant. This point will also be discussed further below.

The last snapshot in Figure 5 shows that even though the confusion of overlapping rings makes their individual identification difficult, a ring wave can still lift the outer disk particles. This gives the appearance of a strong lens component superposed on the disk. This feature is found in all of the simulations presented in this paper.

Many of the qualitative features of Figures 4 and 11 are also seen in the full  $N$ -body calculations of Appleton and James (1989, and private communication) with similar companion/target mass ratio, including the qualitative structure of the ring, the formation of the lenslike component, and the fact that the disk is not perturbed much perpendicular to its plane.

The simulations presented in Figures 4 and 5 were repeated with the softened point-mass potential (eq. [1] with  $p = 1$ ) in place of equation (21). The resulting ring waves and particle distributions in the disk plane resemble Figures 4 and 5 quite closely. There is some difference between the two cases in the direction perpendicular to the disk, in the sense that the heating in that direction and the resulting disk thickness are moderately greater with the softened point-mass potential. This behavior is expected since the gravitational acceleration on a test particle located close to the center ( $r \rightarrow 0$ ) is  $g \propto -|r|\hat{r}$  for a Hubble-like profile, and  $g \propto -\hat{r}$  for a softened point mass ( $\hat{r}$  is the radial unit vector). The greater acceleration in the latter case results in enhanced thickening in the direction perpendicular to the disk. Some other differences in detailed morphology will be discussed below. However, the overall conclusion is that the results discussed above are not particularly sensitive to the exact form of that potential.

### c) Comparison to Analytic Models

In this section we will use the analytic models of § II to help understand the numerical results presented above.

#### i) Particle Orbits and Ring Structure

In order to test the approximations adopted in the kinematic model, we begin by analyzing individual particle orbits from a series of single-component (Hubble-like) simulations. The particle orbits were also used to check the quantitative predictions of equations (5), (6), and (8) for the amplitude, sinusoidal form,

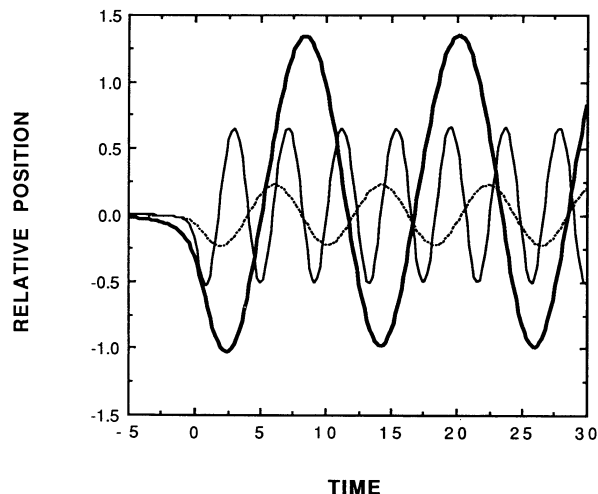


FIG. 6.—Epicyclic oscillations of test particles initially located at  $q = 7.5\gamma$  (solid curve), and  $15.0\gamma$  (thick solid curve) following a collision with a 10% companion. Dashed curve shows the motion of a test particle with  $q = 15\gamma$  following a collision with a 2% mass companion, and where the mass of the target galaxy is twice that of the previous case. The sinusoidal form, the amplitude, and the frequency of all of these curves agree well with the predictions of eqs. (5), (6), and (8).

and frequency of the epicyclic oscillations. The parameters that were varied in the simulations were the initial radius of the test particle, the mass of the main galaxy, and the mass ratio between the companion and the main galaxy. Figure 6 shows the radial motion of several test particles relative to their unperturbed guiding center orbits. The thick and thin solid curves refer to particles with initial radii of  $15\gamma$  and  $7.5\gamma$ , respectively, in the case where  $M_c/M_G = 0.1$ . The dashed curve is for a particle with initial radius of  $15\gamma$  in the case where  $M_c/M_G = 0.02$ , and where the mass of the target galaxy is twice that used previously. The radial oscillations in all the simulations appear to be quite sinusoidal at all times after the impact at  $t = 0$ , in agreement with the epicyclic approximation (eq. [6]). However, note that the radial excursions are not completely symmetric about the initial guiding center radius. This is expected due to the increasing shallowness of the gradient of the effective potential with increasing radius.

The amplitude of the oscillations in our simulations (e.g., compare thick and thin curves in Fig. 6) agrees with that predicted by equation (5), to within 1% as the initial radius of the particle is varied (with all other parameters fixed), and to within less than 10% as the companion-to-target mass ratio is varied over a factor of a few (compare solid and dashed curves in Fig. 6).

The oscillation frequency agrees with that predicted by equation (8) with  $p = 1$  to within  $\frac{1}{2}\%$  as the initial radius is varied (see the thick and thin curves of Fig. 6), and to within 7% when the companion-to-target mass ratio is varied. When the target galaxy mass is increased over a factor of a few, independent of the companion mass, there is always agreement to within 2% between the simulations and equation (8). These comparisons derive from a large number of orbital calculations, but the three examples shown in Figure 6 are representative.

Other comparisons can be made between the collective behavior of the  $10^4$  test particles used in the simulations described in the previous section and the kinematic model. The results include the following:

1. Since the condition that  $A > A_{\min}$  is not met in the first ring ( $A_{\min}^1 = 0.21$  in the outer disk) in the cases shown in both Figures 4 and 5, we do not expect caustics to form in the first ring. At times  $t = 1-3$ , the figures do show that the first ring is a very weak compression with no clear edges. The critical amplitude for caustic formation in the second ring ( $A_{\min}^2 = 0.07$ ) is close to the actual amplitude for the case shown in Figure 4 and is exceeded in the case shown in Figure 5. In both figures, the second ring has clear edges and is stronger and broader in the latter case.

2. The modest broadening of the first few rings as they propagate outward is apparent in both the model predictions and the simulations (compare Figs. 3 and 4).

3. At a given time, there is quite good quantitative agreement between the ring widths predicted by equation (20) and the simulations. For example, at  $t = 6$  in Figures 4 and 5 the second ring has propagated well out into the disk. Solving the condition  $\omega t = 3\pi$  (with  $p = 1$ ) shows that particles within the ring have  $q \approx 8\epsilon$  (or  $\gamma$  as in eqs. [21] and [22]). Then we can use equation (5) for  $A$  and equation (19) for  $\theta$  in equation (20) to estimate the ring width as  $2\Delta r \approx 1.3\epsilon, 2.4\epsilon$ , for  $M_c/M_G = 0.1, 0.2$ , respectively. The actual widths at this time in Figures 4 and 5 are about  $1.0-1.2\epsilon$  and  $1.4-1.7\epsilon$ , respectively. The estimate from equation (20) is quite good in the first case and too large in the second case. In fact, it appears that the approximation that all ring particles have about the same value of the Lagrangian coordinate  $q$  is not accurate in the latter case. A more careful calculation, using the conditions  $\omega t = 2.5\pi, 3.5\pi$  to estimate the lower and upper values of  $q$  within the ring, gives a width estimate of  $1.5\epsilon$ , in good agreement with the simulation results.

4. Figure 3 suggests that when  $A \approx 0.2$ , the third and later rings will be strongly overlapping, while overlap will not occur before about the fifth ring when  $A \approx 0.1$ . These expectations are verified in Figures 4 and 5.

#### ii) The Birth and Propagation of Rings

In general, as discussed in ASZ, pairs of  $A_2$  (fold) singularities are born at a common radius and time as an  $A_3$  singularity or cusp catastrophe. In the present context, an  $A_3$  singularity is defined as satisfying both  $\partial r/\partial q = 0$  (eq. [10]) and  $\partial^2 r/\partial q^2 = 0$  and is effectively the birthplace of a nonlinear ring. Using equation (6) (or differentiating eq. [11]), we get

$$\omega t \tan(\omega t) = \frac{2(\omega/q)}{d\omega/dq} + \frac{\omega(d^2\omega/dq^2)}{(d\omega/dq)^2}. \quad (26)$$

If we define a function  $f_2$  such that

$$\frac{d^2\omega}{dq^2} = \frac{1}{\omega} \left( \frac{d\omega}{dq} \right)^2 - \frac{\omega}{q^2} f_2 \left( \frac{q}{\epsilon} \right), \quad (27a)$$

then

$$f_2 = \frac{B_0 + B_2(q^2/\epsilon^2) + B_4(q^4/\epsilon^4) + B_6(q^6/\epsilon^6) - 3(q^8/\epsilon^8)}{2[(q^2/\epsilon^2) + 1]^2[(q^2/\epsilon^2) + 2p + 1]^2}, \quad (27b)$$

with

$$\begin{aligned} B_0 &= -(3 + 10p + 4p^2 - 8p^3), \\ B_2 &= -2(6 + 11p - 8p^2 - 12p^3), \\ B_4 &= -2(9 + 15p - 2p^2), \\ B_6 &= -6(2 + 3p), \end{aligned}$$

and equation (26) can be written

$$\omega t \tan(\omega t) = \frac{f_1^2 - 2f_1 - f_2}{f_1^2}. \quad (28)$$

This form, like equation (13), reveals clearly the separability of the variables  $\omega t$  and  $q/\epsilon$ . However, there are a couple of important differences between equations (13) and (28). First, equation (28) is a quartic in  $(q/\epsilon)^2$ , rather a quadratic, and so it is not readily solvable. Second, equation (28) has *no amplitude dependence*; the factors of  $A$  cancel in deriving equation (26). Moreover, this fact does not depend on the form of the gravitational potential, i.e.,  $\omega(q)$ , but it is a universal result of the constant-amplitude, free-oscillator model. [Clearly, it is also approximately true for amplitude functions  $A(q)$ , which depend weakly on Lagrangian position  $q$ .]

Both the thickness of the rings and the position of their birth depend on perturbation amplitude through equation (13). After a ring's formation, while solutions to equation (13) mark the ring boundaries, there is at all times a solution to equation (28) for some  $q$  corresponding to a particle located within the interior of the ring which can be viewed as the ring center. Thus, the propagation of a ring center is independent of the (constant) amplitude and depends only on the gravitational potential in the disk. This is confirmed in the simulations with Hubble-like and softened point-mass potentials.

Again it is helpful to consider some limiting cases. First, consider the central regions where  $q/\epsilon \ll 1$ ,  $f_1 \approx (3 - 2p)/2$ ,  $f_2 \approx -(3 + 10p + 4p^2 - 8p^3)/[2(2p + 1)^2]$ . Then when  $p = 1$ , equation (28) reduces to  $\omega t \tan(\omega t) \approx -1$ , with the first few solutions being  $\omega t \approx 0.89\pi, 2.97\pi, 4.98\pi, \dots$  [when  $p = 3/2$ , then  $\omega t \tan(\omega t) \approx 5/9$ ,  $\omega t \approx 1.05\pi, \dots$ ]. Since in this limit  $\omega \propto q^{(2p-3)/2}$  (from eq. [8]), the ring center propagates according to

$$q_{II} \propto t^{2/(3-2p)}, \quad (29)$$

with the subscript II recalling that this is a second derivative condition. Note also that with  $\omega t \approx n\pi$  (for  $n > 1$ ),  $r \approx q$ .

Now consider the (Keplerian) limit  $q/\epsilon \gg 1$ . In this limit  $f_1 \approx 3/2$ ,  $f_2 \approx -3/2$  (independent of  $p$ ), and  $\omega t \tan(\omega t) \approx \frac{1}{3}$ . The first few relevant solutions to this equation are  $\omega t \approx 1.033\pi, 3.011\pi$ , and  $5.007\pi$ . In this limit  $\omega \propto q^{-3/2}$ , so equation (29) is replaced with

$$q_{II} \propto t^{2/3}. \quad (30)$$

Since the phase is nearly the same as before,  $r \approx q$  again, and equation (30) implies a much slower ring propagation rate in the outer disk (see Figs. 3 and 7).

This and most of the other results in this section are also well illustrated by Figure 7. In this figure, the ring boundaries are plotted as solid ( $A = 0.1$ ,  $p = 1$ ) and dashed ( $A = 0.2$ ,  $p = 1$ ) curves, while the approximate ring centers are plotted as dotted curves. The procedure used to determine the ring boundaries is as follows. Recall that previously we concluded that caustics can usually occur only in the intervals  $(2n - 1)\pi - \pi/2 < \omega t < (2n - 1)\pi + \pi/2$ . (These intervals are marked on the  $x$ -axis in Fig. 7.) For any given phase within an allowed interval, equations (13) and (14) can be used to calculate  $q_c$ , the Lagrangian coordinate of the caustic particle at that phase. Then we can divide the phase by  $\omega(q_c)$  as derived from equation (8) to derive  $t$ . Finally, equations (14) and (6) are used to derive  $r_c$ , the caustic position at time  $t$ . To plot the ring centers, we approximated their phase as  $\omega t \approx (2n - 1)\pi$  and

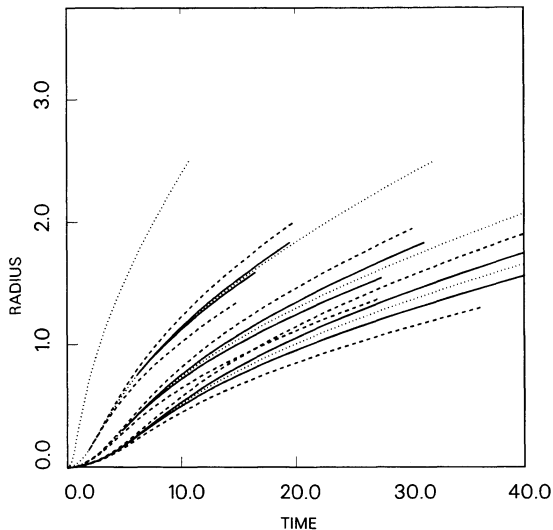


FIG. 7.—Radial propagation of the first four pairs of ring edges ( $A_2$  fold singularities) in the cases with perturbation amplitude  $A = 0.1$  (solid curves) and  $A = 0.2$  (dashed curves), and  $p = 1$ . In both cases, no caustic forms in the first ring, and the separation between the two folds is negligible in the second ring in the small-amplitude case. Dotted curves mark points at the ring center as described in the text.

repeated the above procedure for the center position as a function of time. The increase in ring width amplitude discussed above is obvious in this graph. Also, the position of the ring center is independent of the disturbance amplitude. Recall that in the first ring the caustic condition is not satisfied for  $A = 0.1, 0.2$ , but it is in the second ring. The amplitude dependence of the caustic birthpoint is also evident in the second ring.

### iii) Stellar Densities within Rings

The local star density in the galactic disk is given by equation (9) up to the time of singularity formation. Even after the two caustics have formed, it is apparent from Figure 2 that the equation is still valid within the ring if it is applied piecewise to each of the three star streams discussed above. In the middle (or interior) stream,  $r$  decreases with  $q$ , so the density must be computed from the absolute value of  $dr/dq$ .

In fact, because the phase  $\omega t$  of the ring center is always approximately equal to odd multiples of  $\pi$ , it is especially easy to estimate the density of this middle stream in the ring center. When  $\omega t = (2n - 1)\pi$  ( $n = 1, 2, 3, \dots$ ) and  $r \approx q$ , equations (6), (9), and (12b) yield

$$\frac{\rho_{\text{mid}}}{\rho_0} = \left( \frac{r}{q} \left| \frac{dr}{dq} \right| \right)^{-1} = \frac{1}{|1 - (2n - 1)\pi A f_1|}. \quad (31)$$

A careful examination of Figure 3 reveals that the middle stream is the densest. The density of the incoming stream does not vary rapidly and is therefore roughly the same for ring and inter-ring, so to estimate its value it is sufficient to use the (inter-ring) phase  $\omega t \approx 2(n - 1)\pi$  (see Fig. 3). Then the corresponding density is

$$\frac{\rho}{\rho_0} = \frac{1}{1 + 2(n - 1)\pi A f_1}. \quad (32)$$

Similarly, the phase of the outgoing stream is roughly  $\omega t \approx 2n\pi$ . Thus, the ring density is approximately the sum of

the three stream densities given by equations (31), (32), and (33) below.

The ring density can be contrasted with an estimate of the rarefied inter-ring density at phase  $\omega t = 2\pi n$ ,

$$\frac{\rho_{\text{rare}}}{\rho_0} = \frac{1}{1 + 2\pi n A f_1}. \quad (33)$$

As  $n$  increases, the inter-ring density continually decreases. However, this is often not observable, since as we have seen the higher order rings generally overlap each other, leaving no pure rarefaction region.

Since according to equation (12),  $1.0 < f_1 < 1.5$  for  $q > \epsilon$ , the denominator in equation (31) will take its smallest value in the first ring if  $A$  is greater than about 0.2, yielding the highest density there. Higher order rings with larger values of  $n$  will have lower interior densities. If, on the other hand,  $A \ll 0.1$ , then the quantity in the absolute values will be positive in the first ring, approach zero in the second or later rings, and then become progressively more negative as  $n$  increases further. Thus, the second or later ring will have the maximum interior density. For example, if  $A = 0.02$ , then this argument suggests that the sixth ring has the maximum interior density. Again, restricted three-body simulations confirm these predicted trends.

Quantitative comparison is more difficult, however, for practical reasons which are also relevant to observational comparisons. To make this comparison, we divide the target disk in the simulations into 50 annuli and compute the density within each. In the low-amplitude case ( $A < 0.1$ ), where the rings are thin, this division is sufficient to resolve the rings, but not to make a very accurate estimate of their internal density. If we divide the target disk into many more annuli, then there would be too few particles in each annulus to allow accurate density determinations. This difficulty is less severe in the large-amplitude case, where rings are thicker. However, comparison is still difficult due to the overlapping of the third and later rings, as well as the weakness of the first ring.

Figure 8 shows the run of density in one case where quantitative comparison is possible. This simulation is much like that shown in Figure 5 except with a somewhat larger amplitude of  $A = 0.23$  ( $M_c/M_G = 0.3$ ) and an initial  $1/r$  density profile. The density profile is shown at times of 5 and 7 units, when the second ring is moving toward the outer edge of the disk. Even with the annular averaging, the inner and outer edge caustics of the ring are evident. Apparently, the third ring's edges are also visible, although Figure 5 would lead us to expect some overlap between the third and fourth rings at this time. (Note also that initially the center of the disk had no test particles, which accounts for the density drop there.) In this case, equations (31)–(33) predict a density contrast of 5.0 between the interior of the second ring and the rarefied region behind it and a factor of 1.7 between the densities of the second and third rings. (This is assuming  $q \gg \epsilon$ , so  $f_1 \approx 1.5$ .) The values derived from the numerical calculation are 6.5 for the ring-inter-ring contrast, and 1.3 for the ring-to-ring ratio at  $t = 5$ , and 6.1 and 1.3, respectively, at  $t = 7$ . Thus, these density contrasts stay constant with time as predicted by the analytic model. We can roughly correct for the  $1/r$  initial density profile in the simulations, compared to the flat profile analytic estimates, by multiplying by the ratio of mean ring or inter-ring positions. Then the ring-to-ring density ratio becomes 1.9, and the ring-inter-ring ratio becomes 7.4. Given the roughness of the analytic



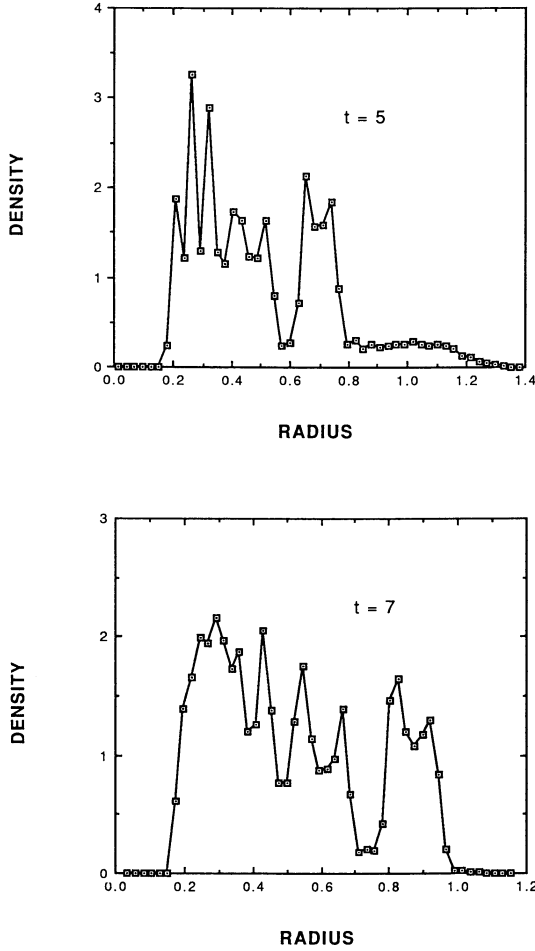


FIG. 8.—Density profiles at two times in the single (bulge) component case, with an initial  $1/r$  density profile. The density unit is arbitrary but is the same in both graphs, while the radius is measured in terms of the initial disk radius.

estimate, these comparisons seem quite good. Note that the small gap followed by a high peak behind the third ring probably indicates overlap between the third and fourth rings.

#### d) Ring Velocities

The equation for the velocity of a caustic is

$$v_c = \frac{dr_c}{dt} = -A\omega q_c \cos(\omega t) + \left[ 1 - A \sin(\omega t) - Aq_c t \cos(\omega t) \right] \frac{d\omega}{dq_c} \frac{dq_c}{dt}. \quad (34)$$

Unfortunately, the expression for  $dq_c/dt$  is too complicated to be useful in closed-form analytic calculations, except in the limiting cases already considered.

#### IV. THE EFFECT OF DISK AND HALO POTENTIALS

In this section we generalize the results of the previous section by presenting numerical simulations in which the target galaxy has a gravitational potential consisting of rigid bulge, disk, and halo components as described in § IIIa. In particular, the inclusion of a flattened disk potential approximates the disk self-gravity. Also, a modest random-velocity component was given to the test particles initially to mimic

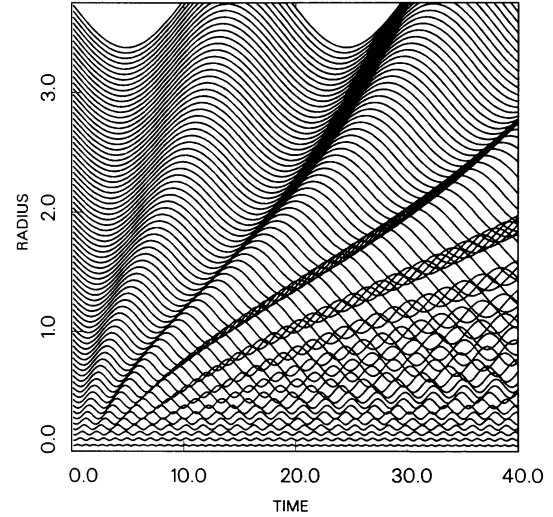


FIG. 9.—Radial trajectories as in Fig. 3, with amplitude  $A = 0.1$ , and a massive halo of characteristic length  $a = 5\epsilon$  (see text).

disk star velocity dispersion. The analytic theory is very messy. Therefore, only a very simple semianalytic example will be discussed, followed by the numerical results. From the outset, we expect that much of the qualitative behavior above will be unchanged, for this behavior consists of the generation and propagation of the basic singularities or catastrophes that are generic to Lagrangian dynamical systems. However, even the details of the evolution of these singularities can have important ramifications for the morphologies of galaxies.

#### a) The Effect of a Halo

A simple way to generalize the softened point-mass bulge is to add a second component, for example, that given by equations (24) and (25), to represent a massive halo. Much of the analytic work above can be straightforwardly generalized to this two-component case. Some of the differences are illustrated in Figure 9, which shows the kinematic trajectories in an example with a perturbation amplitude  $A = 0.1$  and a bulge potential identical to the case shown in Figure 3c, but with an additional halo of mass  $M_h = 10M$  and a scale length  $a = 5\epsilon$ . The time units in Figure 9 are rescaled to the halo free-fall time from a radius  $r = a$ , which allows a better comparison to Figure 3.

First of all, we find that most of the structure within a radius  $r/\epsilon = 2$ , where the bulge dominates, is very similar to the pure bulge example in Figure 3c. Secondly, ring characteristics change at radii between 2 and 4, where the halo potential becomes important. Rings propagate more rapidly, a simple consequence of increased epicyclic frequencies, which results from the large halo mass. The rings also become weaker in the outer regions, indicating a decreasing amplitude  $A$ . This phenomenon contrasts with the results of the previous section, where the amplitude  $A$  remained nearly constant with radius. Using the radial force balance condition (eq. [3]), except with the halo acceleration (eq. [25]) instead of the softened point-mass acceleration, we find that the perturbation amplitude in a pure halo potential, in the limit  $q/a \gg 1$ , is

$$A \approx \frac{1}{2} \frac{M_c}{M_H} \left( \frac{a}{q} \right), \quad (35)$$

where  $a$  is the halo scale-length and  $M_H = 4\pi\rho_0 a^3$ .

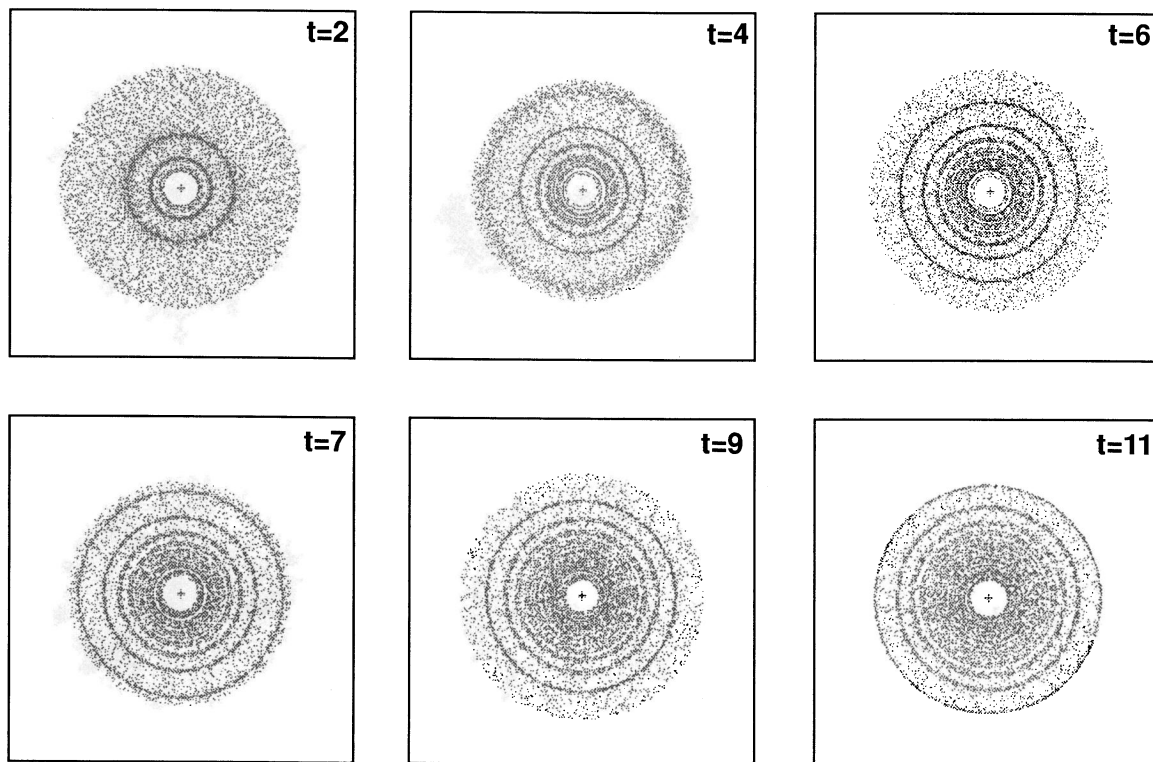


FIG. 10.—Head-on view of a test particle disk in a bulge-disk-halo potential following the central impact of a 10% companion. Time units are the same as in Figs. 4 and 5.

Massive halo examples suggest that galaxies with a faint ring of very large diameter, or galaxies with multiple, widely spaced rings, are likely to possess a massive, extended halo.

#### b) Numerical Results

The analytical work clearly indicates that an extended halo can affect ring morphology. In this section we present several numerical simulations which confirmed the conclusion and give some indication of how it depends on the specific form of the halo potential.

The first of these simulations is shown in Figure 10, which shows snapshots of ring development in a target galaxy with bulge-disk-halo components in the ratio (0.2:1:1) by mass. The scale lengths of the bulge, disk, and halo,  $\gamma$ ,  $\alpha$ , and  $a$ , are 0.05, 0.25, and 0.8 units, respectively. The cutoff radius of the halo is 1.2 units. The companion galaxy has a mass of 10% of the total target mass, it approaches on a slightly hyperbolic orbit, and it impacts perpendicular to the disk at its center. The case shown in Figure 10 is analogous to the single-component case shown in Figure 4. In fact, in comparing the two figures, the overall impression is that the two cases are very similar.

On the other hand, the rings in Figure 10 are generally thinner than those in Figure 4. In Figure 10, the rings have roughly constant width as they propagate outward, in contrast to Figure 4, where rings thicken slightly. This trend is also evident in Figure 11, which shows the results of a simulation exactly like that in Figure 10, but with a 30% mass companion. With equations (6), (17), and (35), we can derive the following expression for the ring half-width in the halo potential,

$$\frac{\Delta r}{a} \approx \frac{1}{2} \frac{M_c}{M_H} \sin(\theta), \quad (36)$$

which predicts no broadening with radius (except possibly through the phase angle  $\theta$ ). Thus, constant width rings seem to be a property of this halo potential.

Comparison of Figures 3, 4, 5, 10, and 11 suggests a few generalizations. First, if three or more stellar rings can be resolved within a disk, then the disturbance amplitude was probably small, i.e., the companion has a relatively low mass (10%). On the other hand, a relatively high mass companion generates a morphology consisting of an outer ring plus a lens (overlapping rings). A similar morphology does appear at late times in a low-amplitude case. These conclusions seem relatively independent of the form of the potential. As noted above, it appears that ring spacing, ring widths, and density contrasts also contain information about the potential as well as the amplitude. Obtaining this information is easier if the age of the rings and the amplitude can be estimated independently from the size of the companion and its distance from the ring.

#### c) Test Particle Orbits

It is interesting to examine the orbits of test particles in the bulge-disk-halo potential, as an extension of the discussion of § IIIc, which dealt with orbits in the single-component potential. This, in turn, provides a better measure of the approximation's relevance to real galaxies. Figures 12a and 12b show the radial and vertical motions of a test particle relative to its unperturbed radial position in the multicomponent potential. In both cases, the particle was initially located at the outer edge of the disk ( $q/a = 1.25$ ). The particles in Figures 12a and 12b are taken from the simulations shown in Figures 10 and 11, respectively.

Like the single-component case shown in Figure 6, the radial oscillations in both Figures 12a and 12b are quite sinusoidal at

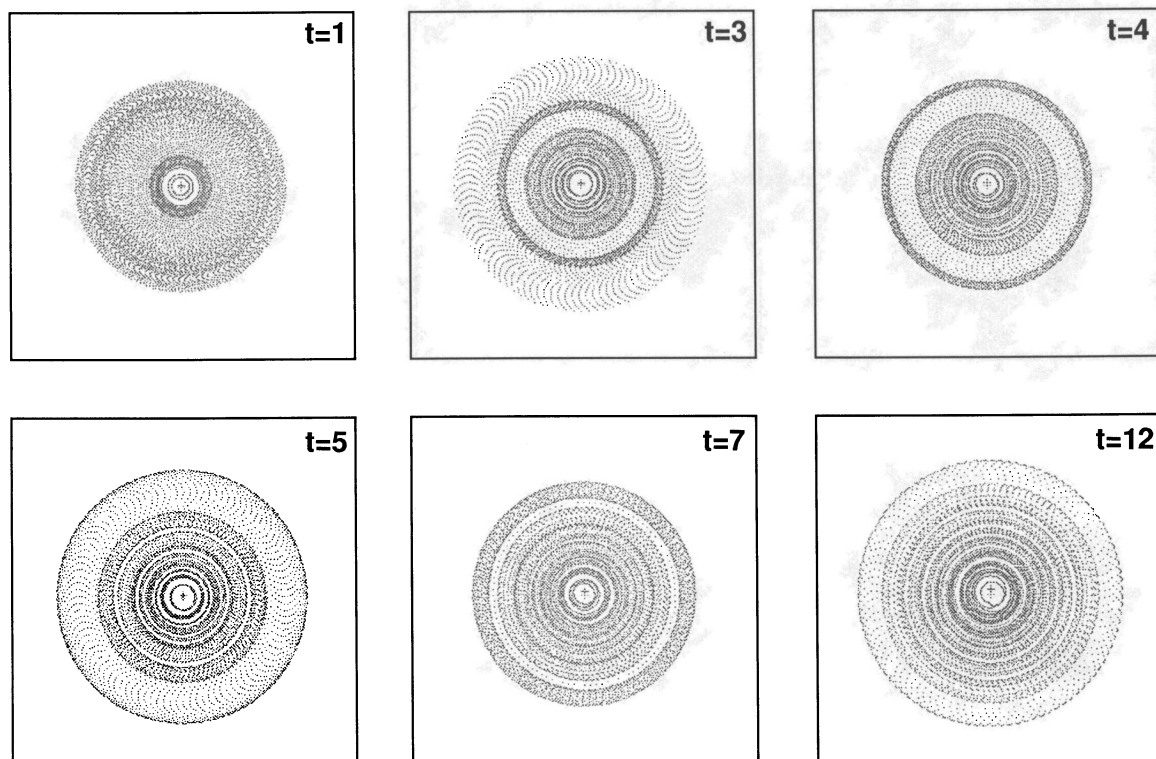


FIG. 11.—Same as Fig. 10, but with a 30% companion

all times after the impact at  $t = 0$ , in agreement with the epicyclic approximation. The oscillation period is found to be about 3.3 time units. In the outer disk, the bulge and disk potentials can be approximated as point masses, and then replacing the first term on the right-hand side of equation (8) with  $G(M_B + M_D)/q^3$ , we derive an analytic estimate of  $P = 3.4$  time units.

The vertical oscillations also have a generally sinusoidal form, but of lower amplitude than the radial ones. Moreover,

the vertical oscillations appear to be modulated on a time scale of several periods, especially in the case shown in Figure 12*b*. In this case, the periods of the vertical and radial oscillations appear to be in a 4:3 resonance, and this is probably the cause of the beating behavior. (The vertical oscillations feel the radial motions through the change in the vertical component of the gravitational force as a function of radius.)

The mean amplitudes of the radial oscillations in Figure 12, and other calculations not shown, are seen to scale roughly as

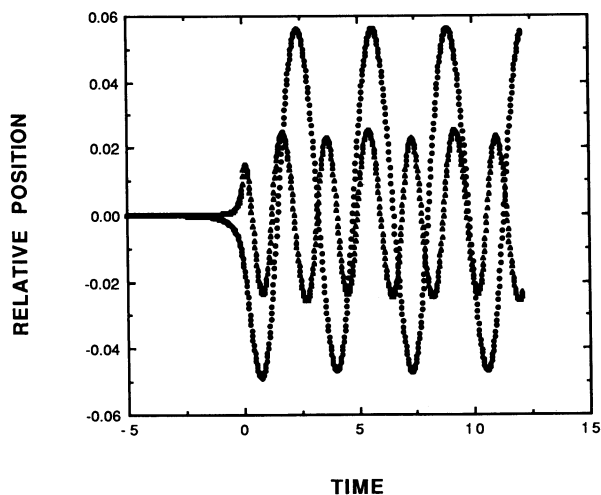
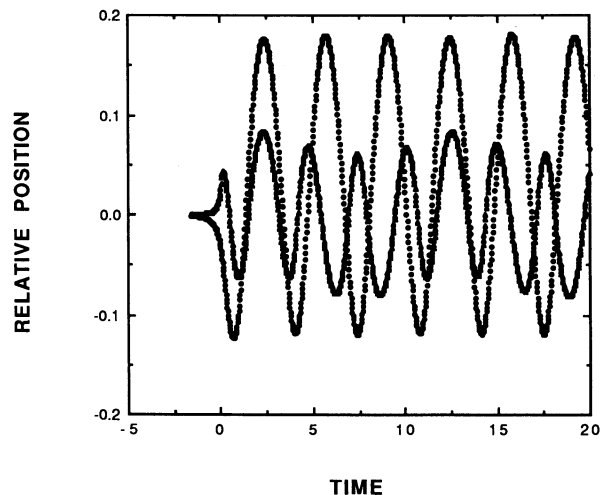
FIG. 12*a*FIG. 12*b*

FIG. 12.—Epicyclic oscillations of a test particle initially located at the outer edge of the disk after a collision with (a) a 10% mass companion, and (b) a 30% mass companion. In both cases, the larger amplitude oscillation corresponds to the radial motion within the disk, and the smaller amplitude oscillation corresponds to the motion perpendicular to the disk.



$M_c/M_G$ , as expected from equation (35) for constant  $q/a$ . We can rederive equation (35) including point-mass approximations for the bulge and disk contributions in the limit  $q/a \gg 1$ , to get

$$A_{\text{BDH}} = \frac{1}{2} \frac{M_c}{M_H} \left( \frac{a}{q} \right) \times \left\{ 1 - \left[ \frac{1}{2} \frac{M_c}{M_H} \left( \frac{M_B + M_D}{M_H} - \frac{\pi}{2} + \frac{1}{2} \frac{M_c}{M_H} \right) \right] \right. \\ \left. \left[ \frac{q}{a} + \frac{1}{2} \left( \frac{M_B + M_D}{M_H} - \frac{\pi}{2} \right) \right] \right\}. \quad (37)$$

For the example shown in Figures 12a and 12b, equation (37) predicts  $A = 0.05, 0.18$ , respectively, in good agreement with the figure.

## V. OBSERVATIONAL COMPARISONS

### a) The Smoothing of Caustics

The fact that the random thermal component of the motion of individual stars will smooth out the density peak in caustics may be an important determinant of the observability of caustics. In this section, a simple quantitative estimate of this effect based on the relevant time scales is derived.

We can estimate the time for stars to diffuse away from the mean flow (which makes up the caustics at the appropriate phase of oscillation) as

$$\tau_d = \frac{\delta r}{c} \approx \frac{Aq}{c} = 1.0 \times 10^9 A \left( \frac{q}{10 \text{ kpc}} \right) \left( \frac{10 \text{ km s}^{-1}}{c} \right) \text{ yr}, \quad (38)$$

where  $\delta r \approx Aq$  is the radial range of the disturbance locally (see eq. [20]), and  $c$  is the thermal velocity. This time scale should be compared to the epicyclic oscillation period  $P$ , derived from equation (8),

$$\frac{\tau_d}{P} = 18A \left( \frac{M}{3 \times 10^{11} M_\odot} \right)^{1/2} \left( \frac{1 \text{ kpc}}{\epsilon} \right)^{1/2} \left( \frac{10 \text{ km s}^{-1}}{c} \right) g \left( \frac{q}{\epsilon} \right),$$

with

$$g = \left\{ \frac{(q/\epsilon)^{2p-1} [(2p+1) + (q^2/\epsilon^2)]}{[1 + (q^2/\epsilon^2)]^{p+1}} \right\}^{1/2}. \quad (39)$$

The function  $g$  ranges in value from a maximum of about 1.0 at  $q/\epsilon = 1.0$ , to  $g \approx (q/\epsilon)^{-1/2}$  at  $q/\epsilon \gg 1$ . Thus it is of order unity or less over the range of interest.

Note that the time scale ratio, equation (39), depends on three dimensionless parameters: (1) the amplitude  $A$ , (2) the ratio of a gravitational potential energy to the thermal energy  $[(GM/\epsilon)/c^2]$  (which is essentially the inverse of the stability parameter  $\alpha$  of star formation theory, or the Ostriker-Peebles [1973]  $t$  parameter), and (3) a structure function  $g$  of the global potential. Of these three, only the second parameter can be much larger than unity, e.g., in a cold disk. Another way to increase this parameter is with a small softening length (e.g., large disk-to-bulge ratio). Alternatively, in a galaxy with significant bulge or halo potential, the effective mass could be several times larger.

Evidently, for reasonable amplitudes (e.g.,  $0.1 < A < 1.0$ ), thermal diffusion and smoothing will be important at all radii, and in many cases it seems likely that the stellar disturbance will begin to smooth away after a few oscillation periods. However, the results of restricted three-body and  $N$ -body simulations with reasonable amounts of thermal energy in the disk assure us that several identifiable rings do develop (see §§ III and IV; Appleton and James 1989 and private

communication), though later rings will be smoothed by caustic broadening and overlap. In very low amplitude perturbations, where caustics are only predicted to develop in high-order rings, smoothing may prevent these rings from appearing. Thermal smoothing will also play an important role in erasing the rings in potentials where there is little ring overlap.

### b) Previous Observations of Ring Structure

The theory above predicts ring widths, ring positions, and relative overdensities in rings as a function of time, form of the target galaxy potential, and collisional amplitude. Assuming that the stellar ring caustics are not promptly smoothed away, several practical difficulties complicate the comparison of theory and observation. The first is distance; there are few nearby cylindrically symmetric rings. The most well-known ring galaxies have diameters of less  $2'$  (see Arp 1966; Arp and Madore 1987; Theys and Spiegel 1976), making high-resolution studies difficult. The second "difficulty" is the vigorous star formation in rings (see, e.g., Theys and Spiegel 1976; Appleton and Struck-Marcell 1987a; Jeske 1986; Majewski 1988). In catalog photos, rings often show a knotty structure. Detailed studies reveal that the knots are young star associations; see, e.g., the Thompson and Theys (1978) study of VII Zw 466, the Few, Madore and Arp (1982) study of the Lindsey-Shapley ring, and the Joy *et al.* (1989) study of the Cartwheel. This is a difficulty in the present context because it means that most of the observational work done to date concerns primarily the young stars and the gas they have formed from. The compressible gasdynamics in rings will be very different than the stellar dynamics (Struck-Marcell and Appleton 1987).

The best way to study the surface density distribution of the old stellar population is with near-infrared photometry. To date, relatively little work of this kind has been published, but see Majewski and Herald (1987), Majewski (1988), and Joy *et al.* (1989). Majewski and Herald did find that rings were "more extended" in the infrared than in the optical. However, Joy *et al.* found that in at least one quadrant of the outer ring the Cartwheel has little or no infrared emission! Neutral hydrogen disks typically extend to larger radii than optical disks in late-type galaxies, and this is also the case in the Cartwheel according to unpublished VLA data of Higdon (1989, private communication). In the Cartwheel, the ring wave may have already propagated out of the stellar disk and may consist of young stars and gas. This is a sobering result in view of the fact that the Cartwheel has become something of a standard ring galaxy since Toomre (1978) first compared his models to it.

A third problem is the presence of stellar bars, which may affect the waves resulting from an otherwise symmetric collision. For example, Taylor and Atherton's (1984) interferometry study of the Vela ring, which has a prominent bar, shows that its kinematics are not compatible with those of a simple rotating, expanding ring. (Moreover, the interferometric observations are detecting the numerous H II regions, not the old stellar population.)

### c) Future Observations

Several workers have undertaken new observations, including near-infrared CCD surface photometry of rings. Specifically, J. L. Higdon has recently obtained data on the Arp 178 system, including the ring galaxy companion (1989, private communication). Appleton and his collaborators have also

obtained near-infrared data on several ring-like systems at the UKIRT facility (1989, private communication). Other systems that we would suggest as possible tests of the caustics theory include, AM 2159—330, AM 0126—680, and AM 0544—393. These systems appear relatively early-type, do not possess a prominent bar, and are sufficiently extended to permit relatively high resolution observations.

The theory above may also apply to some of the Hoag-type galaxies recently discussed by Schweizer *et al.* (1987; also see Struck-Marcell 1990). Although Schweizer *et al.* favor an accretion as the origin of the ring in Hoag's object itself, the galaxies in this class appear very similar to the numerical models presented above. Thus, some of them may be collision remnants.

This example does raise an important point about the comparison of ring theory and observations—there may be more than one way to produce symmetric rings. Accreted material may settle into a symmetric ring, although multiple concentric rings would not be expected in this case. It is also not clear why accretion rings would have sharp caustic edges (although the ring edges do appear relatively sharp in Hoag's object). It is also possible that noncentral collisions could generate symmetric rings. However, a variety of such collisions have been investigated numerically, and most show readily detectable asymmetries (see Toomre 1978; Schweizer 1986; Hernquist and Quinn 1988; Huang and Stewart 1988; Wallin and Struck-Marcell 1988; Appleton and James 1989).

Besides surface photometry, spectra to obtain velocity information across rings would also be very useful. Unfortunately, the picture presented by the stellar velocities in regions of multiple star streams may be complicated. This is a relatively minor problem in narrow rings, like that in Figure 3c, where the stars are moving roughly parallel in all three streams. In broad rings, like those in Figures 3a and 3b, there will be a significant range of positive and negative velocities within a (spatially resolved) ring. If the velocity width is large, and its profile not symmetric, it will be difficult to observe the net radial velocity of the broad ring. To date, most of the analysis of spectra of rings has focused on the H II region emission. It appears that high-quality absorption-line spectra of the old stars would be difficult to obtain.

## VI. CONCLUSIONS

In the preceding sections, we have seen that cylindrically symmetric stellar waves in galaxy disks can evolve in a variety of ways, depending on the amplitude of the perturbation and the potential of the target galaxy. Rings can thicken as they propagate outward (§ III), remain at a nearby constant width (§ IVb), or be pinched off at large radii (§ IVa). Multiple, closely spaced rings can result from a low-amplitude collision (Fig. 3c),

while an outer ring can appear well separated from overlapping inner rings, or an apparent lens structure in halo-dominated potentials (Figs. 9 and 11). (The latter appear relatively common among rings in galaxy catalogs, which may be an argument for the existence of halos in those cases.)

There is great variety among the observed ring galaxies, for example, in the Arp-Madore catalog. The fact that numerical simulations can replicate this variety of form can be considered another success of the Lynds and Toomre collisional model for rings.

Despite the variety of form, however, there is a great deal of simplicity in the rings. First, all the (single-encounter) rings consist of paired fold caustics, i.e., an inner and outer edge, with a high-density interior. Second, the simple (quasi-)impulsive, kinematic oscillation equations (§ II) seem to provide a remarkably accurate model of the numerical simulations. Moreover, simple analytic approximations to these equations allow very good estimates of oscillation periods and amplitudes (even in multiple component potentials), the evolution of ring widths, and ring birth and propagation characteristics. Stellar densities inside and between rings can also be estimated with somewhat less accuracy. The success of the kinematic model implies that it may be an efficient tool for interpreting observations. At the same time, it will be necessary to compare the model to fully self-consistent *N*-body simulations to check the validity of the approximations used. Preliminary comparisons reported above provide some assurances of the relevance of both the kinematic model and the restricted three-body simulations to real ring galaxies.

Other complications remain as well, including: the gas-dynamics, star formation in rings (see Appleton and Struck-Marcell 1987b; Struck-Marcell and Appleton 1987), and especially gas-star interactions. It will require a good deal more numerical and observational work to understand the processes at work in these areas.

C. S. M. is grateful for a visiting fellowship from the Astronomy department of Manchester University in the summer of 1987, and to Franz Kahn for his support and hospitality. Part of the analytic work presented here was begun in the quiet and beautiful environs of Broomcroft Hall there. We wish to thank John F. Wallin for making available to us a restricted three-body code which we extended to accommodate this project. We also wish to thank collaborators Phil Appleton, Richard James, and Althea Wilkinson for many useful discussions, and to express our gratitude to NASA for supporting this work through the grant NAGW 1009. Finally, we are grateful to an anonymous referee for suggestions that lead to substantial improvements of the manuscript.

## REFERENCES

- Alladin, S. M. 1965, *Ap. J.*, **141**, 768.  
 Appleton, P. N., and James, R. A. 1989, preprint.  
 Appleton, P. N., and Struck-Marcell, C. 1987a, *Ap. J.*, **312**, 566.  
 ———. 1987b, *Ap. J.*, **318**, 103.  
 Arnold, V. I. 1972, *Functional Analysis and Applications*, **6**, 254.  
 ———. 1976, *Comm. Pure Appl. Math.*, **29**, 557.  
 ———. 1980, *Mathematical Methods of Classical Mechanics* (New York: Springer-Verlag), Appendix 12.  
 ———. 1984, *Catastrophe Theory* (New York: Springer-Verlag).  
 ———. 1986, *Catastrophe Theory*, 2d English ed. (New York: Springer-Verlag).  
 Arnold, V. I., Gusein-Zade, S. M., and Varchenko, A. N. 1985, *Singularities of Differentiable Maps*, Vol. 1 (Boston: Birkhauser).  
 Arnold, V. I., Shandarin, S. F., and Zel'dovich, Ya. B. 1982, *Geophys. Ap. Fluid Dyn.*, **20**, 111 (ASZ).  
 Arp, H. C. 1966, *Atlas of Peculiar Galaxies* (Pasadena: California Institute of Technology).  
 Arp, H. C., and Madore, B. F. 1987, *A Catalog of Southern Peculiar Galaxies and Associations* (Cambridge: Cambridge University Press).  
 Binney, J., and Tremaine, S. 1987, *Galactic Dynamics* (Princeton: Princeton University Press), pp. 447–450.  
 Chandrasekhar, S. 1943, *Principles of Stellar Dynamics* (Chicago: University of Chicago Press).  
 Chatterjee, T. K. 1987, *Ap. Space Sci.*, **132**, 177.  
 Few, J. M. A., Madore, B. F., and Arp, H. C. 1982, *M.N.R.A.S.*, **199**, 633.  
 Golubitsky, M., and Schaeffer, D. G. 1985, *Singularities and Groups in Bifurcation Theory*, Vol. 1 (New York: Springer-Verlag).  
 Herquist, L., and Quinn, P. 1987, *Ap. J.*, **312**, 1.  
 ———. 1988, *Ap. J.*, **331**, 682.  
 Huang, S.-N., and Stewart, P. 1988, *Astr. Ap.*, **197**, 14.

- Jeske, N. A. 1986, Ph.D. thesis, University of California, Berkeley.
- Joy, M., Tollestrup, E. V., Harvey, P. M., McGregor, P., and Hyland, A. R. 1989, *Bull. AAS*, **20**, 1000.
- Lotan, P., and Struck-Marcell, C. 1990, in preparation.
- Lynds, R., and Toomre, A. 1976, *Ap. J.*, **209**, 382.
- Majewski, S. R. 1988, in *Towards Understanding Galaxies at High Redshift*, ed. R. Kron and A. Renzini (Dordrecht: Reidel), p. 127.
- Majewski, S. R., and Herald, M. 1988, *Bull. AAS*, **19**, 1032.
- Majthay, A. 1985, *Foundations of Catastrophe Theory* (Boston: Pitman).
- Ostriker, J. P., and Peebles, P. J. 1973, *Ap. J.*, **186**, 467.
- Poston, T., and Stewart, I. N. 1978, *Catastrophe Theory and Its Applications* (Boston: Pitman).
- Quinn, P. J. 1984, *Ap. J.*, **274**, 596.
- Saslaw, W. C. 1985, *Gravitational Physics of Stellar and Galactic Systems* (Cambridge: Cambridge University Press), chap. 62.
- Schweizer, F. 1986, *Science*, **231**, 227.
- Schweizer, F., Ford, W. K., Jr., Jedrzejewski, R., and Giovanelli, R. 1987, *Ap. J.*, **320**, 454.
- Shandarin, S. F., and Zel'dovich, Ya. B. 1984, *Phys. Rev. Letters*, **52**, 1488.
- Struck-Marcell, C. 1990, *A.J.*, **99**, 71.
- Struck-Marcell, C., and Appleton, P. N. 1987, *Ap. J.*, **323**, 480 (Paper II).
- Taylor, K., and Atherton, P. A. 1984, *M.N.R.A.S.*, **208**, 601.
- Theys, J. C., and Spiegel, E. A. 1976, *Ap. J.*, **208**, 650.
- Thompson, L. A., and Theys, J. C. 1978, *Ap. J.*, **224**, 796.
- Toomre, A. 1977, in *The Evolution of Galaxies and Stellar Populations*, ed. B. M. Tinsley and R. B. Larson (New Haven: Yale University Observatory), p. 401.
- . 1978, in *IAU Symposium 79, The Large-Scale Structure of the Universe*, ed. M. S. Longair and J. Einasto (Dordrecht: Reidel), p. 109.
- Tremaine, S. 1981, in *The Structure and Evolution of Normal Galaxies*, ed. S. M. Fall and D. Lynden-Bell (Cambridge: Cambridge University Press), p. 67.
- Villumsen, J. V. 1985, *Ap. J.*, **290**, 75.
- Wallin, J. F., and Struck-Marcell, C. 1988, *A.J.*, **96**, 1850.
- White, S. D. M. 1982, in *The Morphology and Dynamics of Galaxies*, ed. L. Martinet and M. Mayor (Sauverny: Geneva Observatory), p. 289.

CURTIS STRUCK-MARCELL and PNINA LOTAN: Astronomy Program, Physics Department, Iowa State University, Ames, IA 50011